RESEARCH ARTICLE | DECEMBER 11 2023

Improving spatial resolution of sunspot HMI images using conditional generative adversarial networks

Agus Prianto; Ridlo Wahyudi Wibowo ✉; Gerhana Puannandra Putri; Ibnu Nurul Huda; Vasyl Yurchyshyn; Hakim Luthfi Malasan

AIP Conf. Proc. 2941, 040009 (2023)
https://doi.org/10.1063/5.0181507

Improving Spatial Resolution of Sunspot HMI Images Using Conditional Generative Adversarial Networks

Agus Prianto,[1] Ridlo Wahyudi Wibowo,[1, 2, 3, 4, a)] Gerhana Puannandra Putri,[5, 6] Ibnu Nurul Huda,[7] Vasyl Yurchyshyn,[8] and Hakim Luthfi Malasan[4, 1, 5, 9]

[1)] *Department of Atmospheric and Planetary Sciences, Institut Teknologi Sumatera, Lampung Selatan, Indonesia*
[2)] *Planetary Science Research Group, Institut Teknologi Sumatera, Lampung Selatan, Indonesia*
[3)] *Artificial Intelligence Research and Innovation Center, Institut Teknologi Sumatera, Lampung Selatan, Indonesia*
[4)] *Observatorium Astronomi ITERA Lampung, Lampung Selatan, Indonesia*
[5)] *Astronomy Study Program, Institut Teknologi Bandung, Bandung, Indonesia*
[6)] *Space Research Center, National Research and Innovation Agency, Bandung, Indonesia*
[7)] *Research Center for Computing, National Research and Innovation Agency, Bogor, Indonesia*
[8)] *Big Bear Solar Observatory of New Jersey Institute of Technology, California, USA*
[9)] *Astronomy Research Group, Institut Teknologi Bandung, Bandung, Indonesia*

[a)] *Corresponding author: ridlo.wibowo@sap.itera.ac.id*

Abstract. Solar Dynamics Observatory (SDO) spacecraft as a space-based project is able to conduct continuous monitoring of the Sun. The Helioseismic and Magnetic Imager (HMI) instrument on SDO, in particular, provides continuum images and magnetograms with a cadence of under 1 minute. SDO/HMI's spatial resolution is only about 1", which makes it impossible to perform a good analysis on the subarcsecond scale. On the other hand, larger aperture ground-based telescopes such as the Goode Solar Telescope (GST) at the Big Bear Solar Observatory are able to achieve a better resolution (16 times better than SDO/HMI). However, ground-based telescopes like GST have limitations in terms of observation time, which can only make observations during the day in clear sky condition. The purpose of this study is to make attempts in improving the spatial resolution of images captured by HMI beyond the diffraction limit of the telescope by employing the Conditional Generative Adversarial Networks algorithm (cGAN). The cGAN model was trained using 1800 pairs of HMI and GST sunspot images. This method successfully reconstruct HMI images with a spatial resolution close to GST images, this is supported by ∼62% increase in the peak signal-to-noise ratio (PSNR) value and ∼90% decrease in the mean squared error (MSE) value. The higher resolution sunspot images produced by this model can be useful for further Solar Physics studies.

INTRODUCTION

Latest solar research shows that solar activity has a significant effect on modern technology. Solar activity events such as Coronal Mass Ejections (CMEs) can cause geomagnetic storms that affect satellite operations, navigation systems [1], as well as the power grid [2]. Therefore, further solar research will play an important role in mitigating and minimizing these effects. Some modern instruments provide us with images of the solar surface depicting pores and sunspots finely structured penumbral filaments and umbral dots. These sub-arcsecond resolution images are needed to provide accurate information and prediction about future solar activity.

Ground-based solar telescopes, because of their size, can produce solar images with higher spatial resolution than existing space-based telescopes. Thus, the Goode Solar Telescope (GST) operating at the Big Bear Solar Observatory (BBSO) routinely produces 0".1 resolution images of the solar photosphere with the pixel size 0".034/pixel [3]. At the same time the Helioseismic and Magnetic Imager (HMI) on board Solar Dynamic Observatory (SDO) acquired photospheric images with the pixel size 0".505/pixel and 1" resolution, indicating that the resolution of the GST data is about one order of magnitude higher than that of HMI instrument. However, ground-based observations have the disadvantage in that they heavily rely on clear skies and good seeing conditions, while space-based instruments are able to collect data of uniform quality during long periods of time, and very often continuously for 24 hours a day.

To overcome this limitation, some methods have been developed to improve the spatial resolution of solar images. Thus, speckle mask method is one of the traditional image reconstruction procedures that can eliminate the atmospheric turbulence effect [4]. However, this method can not increase the image resolution beyond the diffraction limit of the telescope. Recently, deep learning methods have been frequently employed to tackle this problem. This approach utilizes a regression method based on the convolution process that will modify the neural network parameters until the reconstructed image satisfactorily matches the reference image. Thus, [5] used conditional Generative Adversarial Networks (cGAN) to reconstruct HMI images that yield an output with four times the resolution of the original HMI image.

The 9th International Seminar on Aerospace Science and Technology – ISAST 2022
AIP Conf. Proc. 2941, 040009-1–040009-8; https://doi.org/10.1063/5.0181507
Published by AIP Publishing. 978-0-7354-4755-4/$30.00

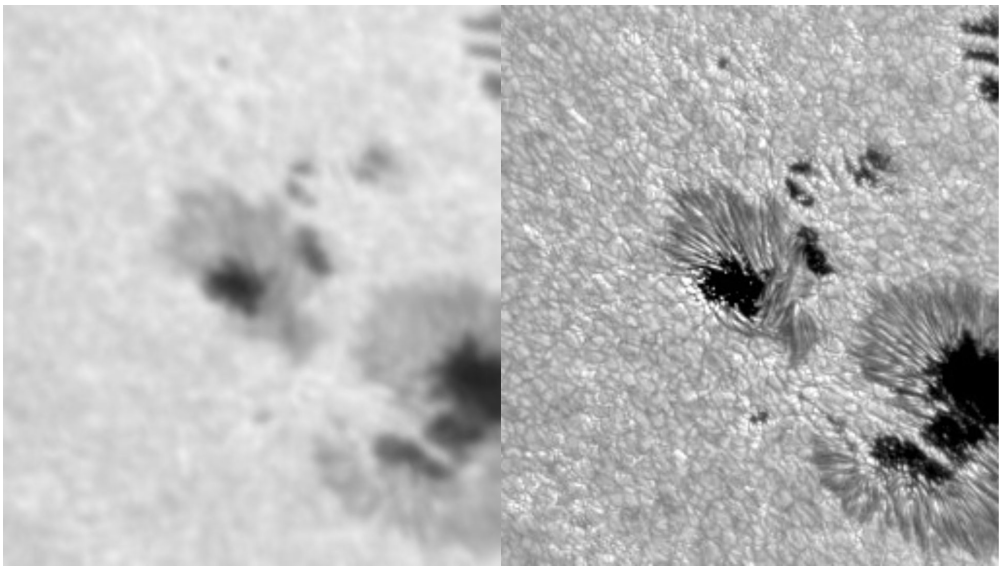

FIGURE 1: Result of alignment of HMI (*left*) and GST images (*right*). The data were acquired on 09 May 2021 at 21:23:02 UTC.

DATASETS

The data used in this research consists of i) solar images taken by GST using the head of the Titanium Oxide (TiO) 705.7 nm molecular band that can be accessed via Big Bear Solar Observatory website (`http://bbso.njit.edu/`) and ii) SDO/HMI continuum intensity images that can be accessed via Stanford Solar Group website (`http://hmi.stanford.edu/`). The dataset training used in this study covers a time interval of nearly 10 years (from 2011 to 2020). We used 60 sunspot images in 2021 representing each sunspot class to test the performance of the cGAN model. The data was arranged in pairs and Figure 1 shows an HMI image is on the left and the corresponding GST image is on the right, with a resolution of 288 x 288 pixels. Before further image processing, we need to extract the sunspot coordinates from the GST image using the SunPy library ([6]) to find the corresponding sunspot in the HMI image. The next step is to align both images with high accuracy. To do so we used the Scale-Invariant Feature Transform (SIFT) method from OpenCV Library [7] [8].

To implement SIFT, we need to identify a key-point as a reference, match the key-point, and then determine the registration parameter. Noise reduction also needs to be done by using gaussian blurring, to decrease the probability of noise feature used as the key-point. Rotation, translation, and scale (RTS) values can be obtained by comparing the adjacent layers of the multi-scale gaussian pyramids. Image matching was assessed from the relationship between the feature point descriptors in the two images. The problem that often occurs is that this relationship is not strong. It can be overcome by implementing the nearest neighbor method that is used to minimize the Euclidean distance between the descriptor and the feature point. When the ratio of the closest distance to the second closest Euclidean distance is less than a predetermined threshold value, the feature point will be considered a match. The last stage is image registration, which is the process of converting different data sets into the same coordinate system. To get the equation of homogeneous coordinate transformation, we need to connect the feature points of the two images. In the process of solving it, we use the consensus sampling algorithm (RANSAC) to overcome the problem of unstable feature points.

For training process we selected 450 HMI-GST pairs since GST observations not always included a sunspot in their field of view. To increase variations in the training data, data augmentation was carried out by applying vertical and horizontal flip, as well as 180-degree rotation to the main data so that a total of 1800 HMI-GST image pairs were obtained.

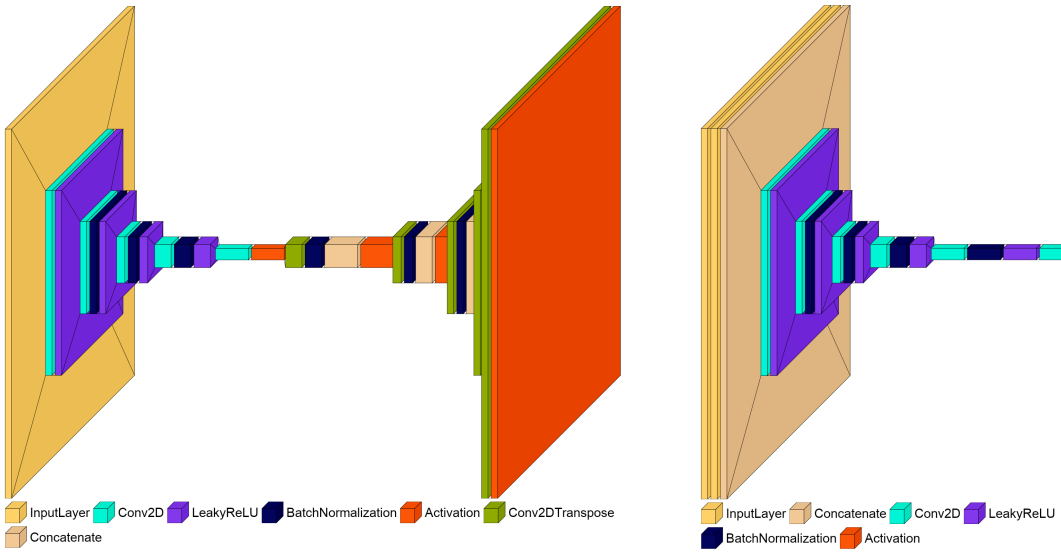

(a) Generator (b) Discriminator

FIGURE 2: Generator network structure (a) is divided into the downsampling part of feature extraction and the upsampling part of the feature fusion. The input layer in the generator is an HMI image. Discriminator network structure (b) classifies the generated and target images; returns the evaluation for generated image as a fake or real image.

TABLE I: Structure of the Neural Network

Structure	Layer	Filter	Strides	Normalization	Activation	Output Size
Generator	Input Layer	-	-	-	-	$288 \times 288 \times 3$
	Conv 64	4×4	2×2	-	Leaky ReLU	$144 \times 144 \times 64$
	Conv 128	4×4	2×2	Batch Norm	Leaky ReLU	$72 \times 72 \times 128$
	Conv 256	4×4	2×2	Batch Norm	Leaky ReLU	$36 \times 36 \times 256$
	Conv 512	4×4	2×2	Batch Norm	Leaky ReLU	$18 \times 18 \times 512$
	Conv 1024	4×4	2×2	-	ReLU	$9 \times 9 \times 1024$
	ConvT 512	4×4	2×2	Batch Norm	ReLU	$18 \times 18 \times 512$
	ConvT 256	4×4	2×2	Batch Norm	ReLU	$36 \times 36 \times 256$
	ConvT 128	4×4	2×2	Batch Norm	ReLU	$72 \times 72 \times 128$
	ConvT 64	4×4	2×2	Batch Norm	ReLU	$144 \times 144 \times 64$
	ConvT 3	4×4	2×2	Batch Norm	tanh	$288 \times 288 \times 3$
Discriminator	Input Layer	-	-	-	-	$288 \times 288 \times 3$
	Concat	-	-	-	-	$288 \times 288 \times 6$
	Conv 64	4×4	2×2	-	Leaky ReLU	$144 \times 144 \times 64$
	Conv 128	4×4	2×2	Batch Norm	Leaky ReLU	$72 \times 72 \times 128$
	Conv 256	4×4	2×2	Batch Norm	Leaky ReLU	$36 \times 36 \times 256$
	Conv 512	4×4	2×2	Batch Norm	Leaky ReLU	$18 \times 18 \times 512$
	Conv 1024	4×4	2×2	Batch Norm	Leaky ReLU	$9 \times 9 \times 1024$
	Conv 1024	4×4	1×1	Batch Norm	Leaky ReLU	$9 \times 9 \times 1024$
	Conv 1	4×4	1×1	-	sigmoid	$9 \times 9 \times 1$

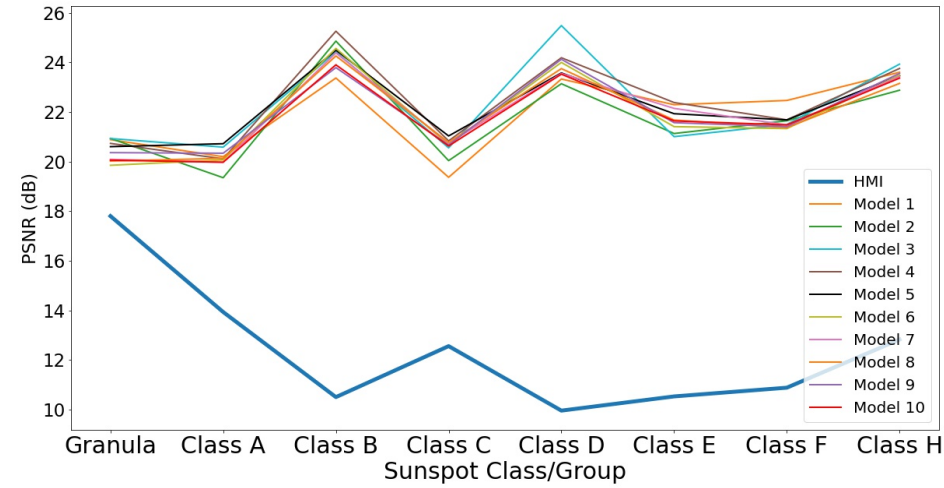

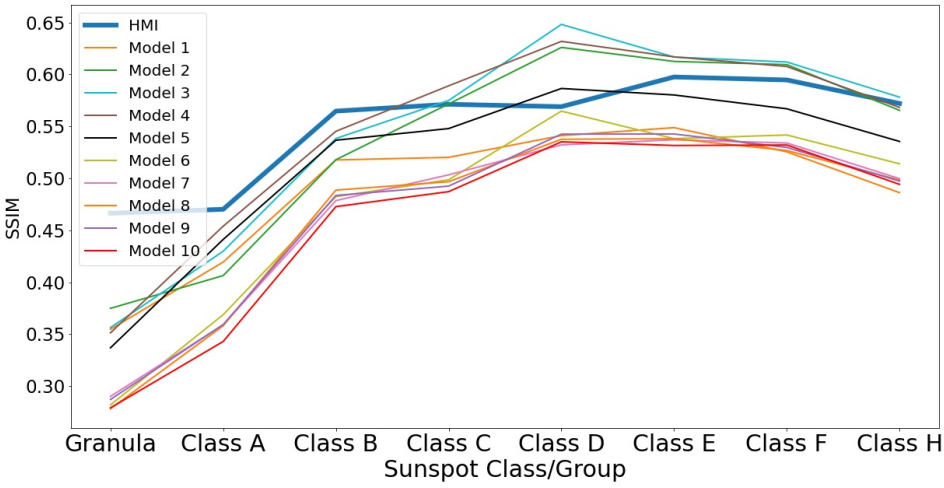

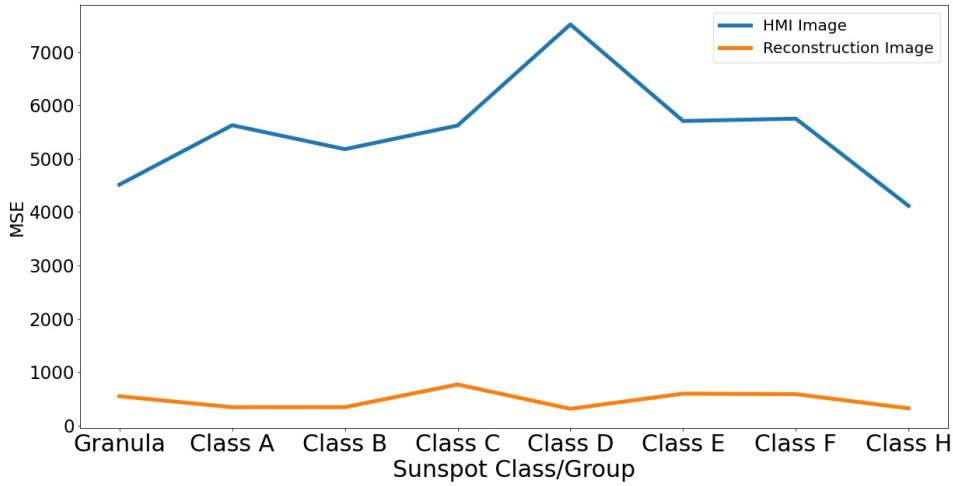

FIGURE 3: PSNR, SSIM, and MSE value of the reconstructed images for the 10 final models compared to the PSNR, SSIM, and MSE value of HMI images.

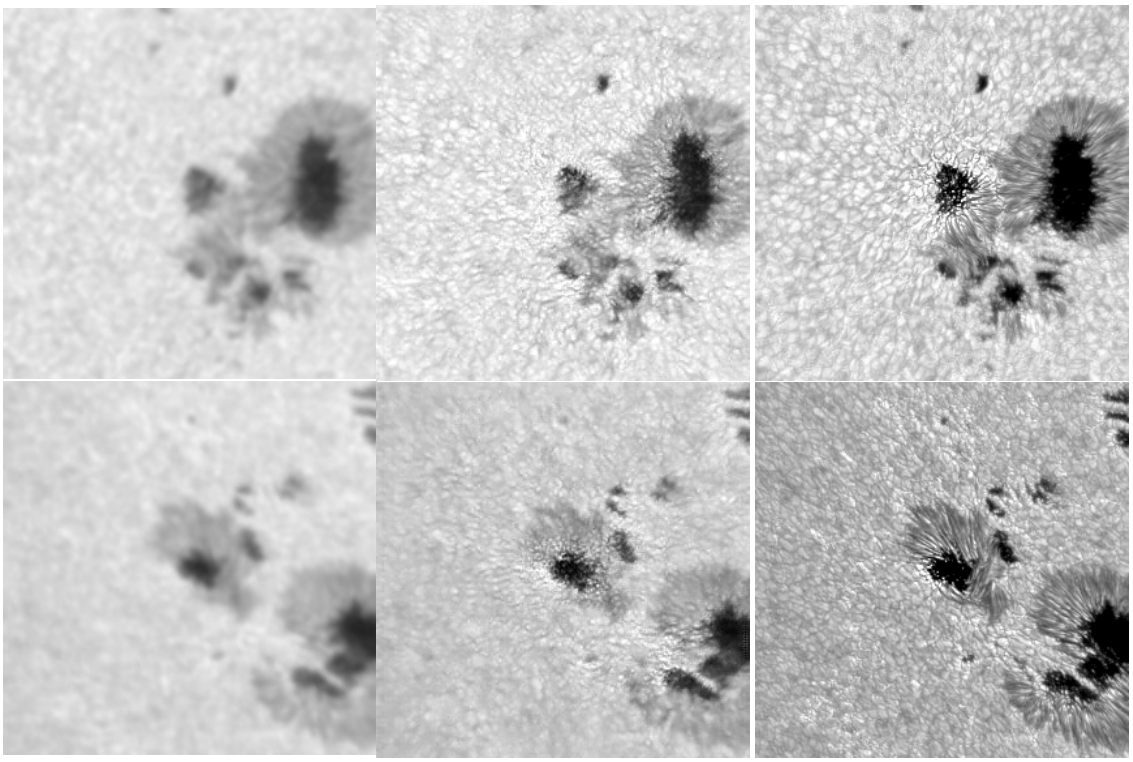

(a) HMI image (input) (b) Reconstructed image (c) GST image (target)

FIGURE 4: Testing results, 2 out of 60 images from 09 May 2021 at 21:23:02 UTC and 12 May 2021 at 18:57:08 UTC. The images from the left shows the HMI image (a), reconstructed image (b), and GST image (c) respectively. The contrast and brightness of the reconstructed images are consistent with the GST images.

METHODS

Network Structure

This study only uses the cGAN algorithm without any Self-Attention optimization as done by J. Deng et al which became our reference paper in this study. A Conditional Generative Adversarial Network (cGAN) [9] was utilized to reconstruct sunspot images. A low resolution (LR) HMI images were used as input to generate or reconstruct a higher resolution (HR) image similar to a target GST image. The basic structure of the generator follows the U-Net, which is suitable for scenes with similar structures between input and output images. The unique structure allows the network to transmit contextual information to higher layers for full integration. The shallow feature map usually contains low-frequency information of the image, such as the overall information of the image. The deep feature maps usually contain high-frequency information of the image, such as the edges and textures of the image. U-Net cascades high-level features and low-level features together through skip connection so that different levels of detailed information can be well preserved and integrated. cGAN consist of two networks: generator which generates an image from an input image and a simple classifier called discriminator.

The generator structure applies an autoencoder model consisting of an encoder and a decoder layer. The encoder layer is composed of convolution kernel with size 4, strides 2, normal random initializer kernel with standard deviation 0.02, padding same, batch normalization, and LeakyReLU (rectified linear activation function/unit) activation function with alpha 0.2. While the decoder layer is composed of a deconvolution kernel with size 4, strides 2, a normal random initializer kernel with a standard deviation of 0.02, padding same, batch normalization, and ReLU activation function. The last layer of the decoder implements the tanh activation function. The optimization of the generator model uses Adam with a learning rate of 0.0002 and a beta of 0.5.

The discriminator model is composed of a convolution layer with size 4, strides 2, normal random kernel initializer

with a standard deviation of 0.02, padding same, batch normalization, and sigmoid activation function. Optimizing the discriminator model using Adam with a learning rate of 0.0002, and beta 0.5, the loss function used is binary cross-entropy. The network structure for generator and descriminator is described in Figure 2.

Evaluation Metrics

For this work, we apply two evaluation metrics/methods to measure the quality of the reconstructed images produced by the models. The first method is visual inspection, which is done by directly comparing the original HMI and GST images, and the reconstructed images. The evaluation criteria includes: (1) how well the reconstructed images can return the detail information found in HMI images, (2) contrast of the intergranular lanes, which are boundaries between photospheric granules, (3) consistency of the contrast and brightness of GST and the reconstructed images, and (4) sharpness of the reconstructed images.

The second method is carried out by implementing quantitative evaluation using three indicators: (1) Peak Signal to Noise Ratio (PSNR) [10], which measures the ratio between the maximum possible power of a signal and the power of corrupting noise, (2) Structural Similarity Index Measure (SSIM) [11] that is used to measure contrast, brightness, and structural details in images, and (3) Mean Squared Error (MSE) that is usually used to check the estimated value of the pixel prediction error against the actual value.

The PSNR value is determined by the maximum pixel value MAX_I of the image and the pixel mean square error (MSE) between I_{LR} and I_{HR}.

$$\mathrm{PSNR} = 10 \cdot \log_{10} \left(\frac{MAX_I^2}{\mathrm{MSE}} \right) \tag{1}$$

with

$$\mathrm{MSE} = \frac{1}{m\,n} \sum_{i=0}^{m-1} \sum_{j=0}^{n-1} [I_{LR}(i,j) - I_{HR}(i,j)]^2. \tag{2}$$

PSNR is the ratio between the maximum possible power of a signal and the power of corrupting noise that affects the fidelity of its representation. Because many signals have a very wide dynamic range, PSNR is usually expressed as a logarithmic quantity using the decibel scale. A higher PSNR generally indicates that the reconstruction is of higher quality. PSNR only focuses on pixel differences and does not consider structural information in the image.

The other indicator that usually used is the Structural Similarity Index Measure (SSIM) which is used to measure contrast, brightness, and structural detail in both images.

$$\mathrm{SSIM}(LR, HR) = \frac{(2\mu_{LR}\mu_{HR} + c_1)(2\sigma_{LRHR} + c_2)}{(\mu_{LR}^2 + \mu_{HR}^2 + c_1)(\sigma_{LR}^2 + \sigma_{HR}^2 + c_2)} \tag{3}$$

The brightness and contrast are obtained by calculating the average (μ) and standard deviation (σ) of image pixels. c_1 and c_2 are constant. μ_{LRSR} represents the covariance of I_{LR} and I_{HR}. SSIM assigns a rating to the image with a range of 0 to 1, where a value of 1 indicates that the two images are very similar or the same. While the value 0 indicates the two images are very different.

RESULTS AND DISCUSSIONS

This study uses cloud computing with specifications of 25 GB RAM and GPU T4 from google colaboratory pro which runs for 7 hours. The programming language used Python version 3.7.13 with supporting libraries for sunpy 3.1.16, astropy 4.3.1, and OpenC 4.5.5.64.

In this project, the model training was conducted for 100 epochs/cycles. One cycle is considered completed when the entire data set has gone through the training process. Each cycle produced a model that can be used to reconstruct solar images. However, instead of saving the entire model for every cycle, we stored one model for every 10th cycle, hence, generating 10 final models, which were used to analyse the change in the model's performance during the training. We used 60 images of different sunspots as a test sample. Due to the limitation in the number of GST images,

TABLE II: The average of changes in PSNR, SSIM, and MSE scores as the performance indicators of the model. The increase of PSNR value and the decrease of MSE score shows the improvement of the image. On the contrary, the decrease of SSIM value indicates the decline of the similarity of the reconstructed image with GST.

Sunspot Class	Number of sample	ΔPSNR	ΔSSIM	ΔMSE
Regions without sunspots	14	12%	-40%	-87%
Class A	2	18%	-44%	-93%
Class B	6	117%	-18%	-93%
Class C	8	67%	-16%	-86%
Class D	5	132%	-7%	-95%
Class E	5	113%	-12%	-89%
Class F	11	98%	-11%	-89%
Class H	9	88%	-12%	-92%

we have a different number of test images for each class of sunspots. Using visual inspection, all criteria presented in Evaluation Metrics subsection were achieved for all 60 test images.

Figure 3 plots PSNR, SSIM, and MSE values for each of the models and HMI images, which demonstrate a good images reconstruction with ∼67% increase in the average PSNR value and ∼90% decrease in the average MSE score. These results show that the reconstructed image structure is closer to the target GST image as compared to the HMI image. We see, however, an average decline of ∼22% in the SSIM indicator. One plausible explanation is that the matching process between HMI and GST images is not perfect. Other possibility is that the SSIM is inherently not suitable to be used as a performance indicator in this type of image since it may create non-intuitive results [12]. This, for example, may happen for low luminance values or when the local distribution of pixel values visually differ very little, though regularly. These criteria are applied for solar surface images.

We grouped the test result based on the sunspot classes to inspect the correlation between the performance of the model and the sunspot classes. Shown in Table II that the models perform better on sunspot class D, E, F, and H compared to the other classes. It is evident from a very high increase in the PSNR value, ranging between 88%-132%, which demonstrates the models' excellent ability to increase the dynamic range of these sunspot images. This is also supported by the magnitude of the SSIM index that declines only slightly from 7% to 12%, indicating no significant difference between GST's and the reconstructed images. Figure 4 shows the test result for the last model for 2 sunspot images. It shows that the contrast and brightness of the reconstructed images are consistent with the GST images.

CONCLUSIONS

From the visual inspection, it is shown that the cGAN model provides good performance. The model is able to restore the granular structure in the HMI image and provide consistent contrast and brightness with the GST image. This is also supported by the PSNR indicator, with the average PSNR value for reconstructed images increased by 67% compared to the average PSNR value for HMI images. However, the SSIM indicator shows a decrease in the quality of the reconstructed image by 22% when we compared it to the average value of the SSIM of HMI images. The value of PSNR and SSIM also shows that the model does not perform well for sunspot images which are dominated by granules structure, such as granule images (no sunspot region), class A, B, and C. One of the possible explanation is the error in image matching process, i.e. the HMI image is not fully matched with the GST image for these classes. Other explanation is that SSIM is inherently not suitable as an indicator when we work with solar surface images [12]. Comparing similar studies conducted by J. Deng et al., it was found that increasing the spatial resolution of the sunspot image has better results if, using an optimized cGAN algorithm using Self-Attention. This is shown in the metric PSNR evaluation was able to increase up to 82% and SSIM increased by 3%, this is far from the results obtained when using the original cGAN algorithm. In the future work we will add larger datasets, improve the image matching process, and try different network structure.

ACKNOWLEDGMENTS

We gratefully acknowledge the use of data from the Goode Solar Telescope (GST) of the Big Bear Solar Observatory (BBSO). BBSO operation is supported by US NSF AGS-1821294 grant and New Jersey Institute of Technology. GST operation is partly supported by the Korea Astronomy and Space Science Institute and the Seoul National University. This research use several open source packages i.e. Sunpy, Matplotlib, Astropy, OpenCV, TensorFlow, and Keras.

REFERENCES

1. M. Hapgood, *Space Weather*, 2399-2891 (IOP Publishing, 2017).
2. C. Balch, B. Murtagh, L. D. Zezula, L. Combs, G. Nelson, K. Tegnell, M. Crown, B. McGehan, J. Kunches, K. Doser, T. Onsager, M. Golightly, J. Kappenman, D. Webb, J. Allen, and H. Keyser, *Service Assessment: Intense Space Weather Storms October 19 - November 07, 2003* (Department of Commerce, USA, 2004) p. 60.
3. P. R. Goode, V. Yurchyshyn, W. Cao, V. Abramenko, A. Andic, K. Ahn, and J. Chae, "Highest Resolution Observations of the Quietest Sun," **714**, L31–L35 (2010).
4. D. A. Hope, S. M. Jefferies, M. Hart, and J. G. Nagy, "High-resolution speckle imaging through strong atmospheric turbulence," Opt. Express **24**, 12116–12129 (2016).
5. J. Deng, W. Song, D. Liu, Q. Li, G. Lin, and H. Wang, "Improving the spatial resolution of solar images using generative adversarial network and self-attention mechanism," The Astrophysical Journal **923**, 76 (2021).
6. The SunPy Community, W. T. Barnes, M. G. Bobra, S. D. Christe, N. Freij, L. A. Hayes, J. Ireland, S. Mumford, D. Perez-Suarez, D. F. Ryan, A. Y. Shih, P. Chanda, K. Glogowski, R. Hewett, V. K. Hughitt, A. Hill, K. Hiware, A. Inglis, M. S. F. Kirk, S. Konge, J. P. Mason, S. A. Maloney, S. A. Murray, A. Panda, J. Park, T. M. D. Pereira, K. Reardon, S. Savage, B. M. Sipőcz, D. Stansby, Y. Jain, G. Taylor, T. Yadav, Rajul, and T. K. Dang, "The sunpy project: Open source development and status of the version 1.0 core package," The Astrophysical Journal **890**, 68– (2020).
7. D. Lowe, "Object recognition from local scale-invariant features," in *Proceedings of the Seventh IEEE International Conference on Computer Vision*, Vol. 2 (1999) pp. 1150–1157 vol.2.
8. G. Bradski, "The OpenCV Library," Dr. Dobb's Journal of Software Tools (2000).
9. P. Isola, J.-Y. Zhu, T. Zhou, and A. A. Efros, "Image-to-image translation with conditional adversarial networks," (2016).
10. Q. Huynh-Thu, English"Scope of validity of psnr in image/video quality assessment," Electronics Letters **44**, 800–801(1) (2008).
11. Z. Wang, A. Bovik, H. Sheikh, and E. Simoncelli, "Image quality assessment: from error visibility to structural similarity," IEEE Transactions on Image Processing **13**, 600–612 (2004).
12. J. Nilsson and T. Akenine-Möller, "Understanding ssim," (2020).
13. R. Wachter, J. Schou, M. C. Rabello-Soares, J. W. Miles, T. L. Duvall, and R. I. Bush, "Image Quality of the Helioseismic and Magnetic Imager (HMI) Onboard the Solar Dynamics Observatory (SDO)," Solar Physics **275**, 261–284 (2012).
14. F. Chollet *et al.*, "Keras," `https://keras.io` (2015).
15. Astropy Collaboration, T. P. Robitaille, E. J. Tollerud, P. Greenfield, M. Droettboom, E. Bray, T. Aldcroft, M. Davis, A. Ginsburg, A. M. Price-Whelan, W. E. Kerzendorf, A. Conley, N. Crighton, K. Barbary, D. Muna, H. Ferguson, F. Grollier, M. M. Parikh, P. H. Nair, H. M. Unther, C. Deil, J. Woillez, S. Conseil, R. Kramer, J. E. H. Turner, L. Singer, R. Fox, B. A. Weaver, V. Zabalza, Z. I. Edwards, K. Azalee Bostroem, D. J. Burke, A. R. Casey, S. M. Crawford, N. Dencheva, J. Ely, T. Jenness, K. Labrie, P. L. Lim, F. Pierfederici, A. Pontzen, A. Ptak, B. Refsdal, M. Servillat, and O. Streicher, "Astropy: A community Python package for astronomy," **558**, A33 (2013), arXiv:1307.6212 [astro-ph.IM].
16. Astropy Collaboration, A. M. Price-Whelan, B. M. Sipőcz, H. M. Günther, P. L. Lim, S. M. Crawford, S. Conseil, D. L. Shupe, M. W. Craig, N. Dencheva, A. Ginsburg, J. T. Vand erPlas, L. D. Bradley, D. Pérez-Suárez, M. de Val-Borro, T. L. Aldcroft, K. L. Cruz, T. P. Robitaille, E. J. Tollerud, C. Ardelean, T. Babej, Y. P. Bach, M. Bachetti, A. V. Bakanov, S. P. Bamford, G. Barentsen, P. Barmby, A. Baumbach, K. L. Berry, F. Biscani, M. Boquien, K. A. Bostroem, L. G. Bouma, G. B. Brammer, E. M. Bray, H. Breytenbach, H. Buddelmeijer, D. J. Burke, G. Calderone, J. L. Cano Rodríguez, M. Cara, J. V. M. Cardoso, S. Cheedella, Y. Copin, L. Corrales, D. Crichton, D. D'Avella, C. Deil, É. Depagne, J. P. Dietrich, A. Donath, M. Droettboom, N. Earl, T. Erben, S. Fabbro, L. A. Ferreira, T. Finethy, R. T. Fox, L. H. Garrison, S. L. J. Gibbons, D. A. Goldstein, R. Gommers, J. P. Greco, P. Greenfield, A. M. Groener, F. Grollier, A. Hagen, P. Hirst, D. Homeier, A. J. Horton, G. Hosseinzadeh, L. Hu, J. S. Hunkeler, Ž. Ivezić, A. Jain, T. Jenness, G. Kanarek, S. Kendrew, N. S. Kern, W. E. Kerzendorf, A. Khvalko, J. King, D. Kirkby, A. M. Kulkarni, A. Kumar, A. Lee, D. Lenz, S. P. Littlefair, Z. Ma, D. M. Macleod, M. Mastropietro, C. McCully, S. Montagnac, B. M. Morris, M. Mueller, S. J. Mumford, D. Muna, N. A. Murphy, S. Nelson, G. H. Nguyen, J. P. Ninan, M. Nöthe, S. Ogaz, S. Oh, J. K. Parejko, N. Parley, S. Pascual, R. Patil, A. A. Patil, A. L. Plunkett, J. X. Prochaska, T. Rastogi, V. Reddy Janga, J. Sabater, P. Sakurikar, M. Seifert, L. E. Sherbert, H. Sherwood-Taylor, A. Y. Shih, J. Sick, M. T. Silbiger, S. Singanamalla, L. P. Singer, P. H. Sladen, K. A. Sooley, S. Sornarajah, O. Streicher, P. Teuben, S. W. Thomas, G. R. Tremblay, J. E. H. Turner, V. Terrón, M. H. van Kerkwijk, A. de la Vega, L. L. Watkins, B. A. Weaver, J. B. Whitmore, J. Woillez, V. Zabalza, and Astropy Contributors, "The Astropy Project: Building an Open-science Project and Status of the v2.0 Core Package," **156**, 123 (2018), arXiv:1801.02634 [astro-ph.IM].
17. J. D. Hunter, "Matplotlib: A 2d graphics environment," Computing in Science & Engineering **9**, 90–95 (2007).